

Published in final edited form as:

Ann Biomed Eng. 2010 December ; 38(12): 3550–3571. doi:10.1007/s10439-010-0110-7.

Numerical study of high frequency oscillatory air flow and convective mixing in a CT-based human airway model

Jiwoong Choi^{1,2}, Guohua Xia^{1,2}, Merryn H. Tawhai⁶, Eric A. Hoffman^{3,4,5}, and Ching-Long Lin^{1,2,*}

¹Department of Mechanical and Industrial Engineering, The University of Iowa, Iowa City, Iowa 52242 ²Department of IHR-Hydroscience & Engineering, The University of Iowa, Iowa City, Iowa 52242 ³Department of Biomedical Engineering, The University of Iowa, Iowa City, Iowa 52242 ⁴Department of Medicine, The University of Iowa, Iowa City, Iowa 52242 ⁵Department of Radiology, The University of Iowa, Iowa City, Iowa 52242 ⁶Bioengineering Institute, The University of Auckland, Auckland, New Zealand

Abstract

High frequency oscillatory ventilation (HFOV) is considered an efficient and safe respiratory technique to ventilate neonates and patients with acute respiratory distress syndrome. HFOV has very different characteristics from normal breathing physiology, with a much smaller tidal volume and a higher breathing frequency. In this work, the high frequency oscillatory flow is studied using a computational fluid dynamics (CFD) analysis in three different geometrical models with increasing complexity: a straight tube, a single-bifurcation tube model, and a computed-tomography (CT)-based human airway model of up to seven generations. We aim to understand the counter-flow phenomenon at flow reversal and its role in convective mixing in these models using sinusoidal waveforms of different frequencies and Reynolds numbers. Mixing is quantified by the stretch rate analysis. In the straight-tube model, coaxial counter flow with opposing fluid streams is formed around flow reversal, agreeing with an analytical Womersley solution. However, counter flow yields no net convective mixing at end cycle. In the single-bifurcation model, counter flow at high Re is intervened with secondary vortices in the parent (child) branch at end expiration (inspiration), resulting in an irreversible mixing process. For the CT-based airway model three cases are considered, consisting of the normal breathing case, the high-frequency-normal-Re case, and the HFOV case. The counter-flow structure is more evident in the high-frequency-normal-Re case than the HFOV case. The instantaneous and time-averaged stretch rates at the end of two breathing cycles and in the vicinity of flow reversal are computed. It is found that counter flow contributes about 20% to mixing in HFOV.

Keywords

high frequency oscillatory ventilation; CT-based human airway; CFD; secondary flow; stretch rate; mixing

Introduction

Ventilatory support via invasive mechanical ventilation is often necessary for patients in an intensive care unit. Conventionally, the tidal volume of normal mechanical ventilation is

*Corresponding author: Ching-long Lin, ching-long-lin@uiowa.edu, Tel: +1 319 335 5673 .

approximately 75 to 150 percent of the patient's natural respiration volume²⁶ based on the prediction that gas exchange volume has to exceed the anatomical dead space (the volume of conducting airways) of the lung to achieve adequate alveolar ventilation. However, this large tidal volume can cause volutrauma (over-stretch of lung tissue) and other ventilator-induced lung injuries (VILI) including oxygen toxicity (the effect of over-rich levels of oxygen on lung tissue), and hemodynamic compromises.^{7,37} To avoid lung injuries due to volutrauma, high frequency ventilation (HFV) with smaller tidal volume has been used on patients with acute lung injury (ALI), acute respiratory distress syndrome (ARDS), and neonates. HFV is a fast and shallow ventilation mode which is postulated to minimize the lung injuries associated with cyclic opening and closing of alveolar units in conventional ventilation mode.¹⁵ HFV includes high frequency positive pressure ventilation, high frequency jet ventilation and high frequency oscillatory ventilation (HFOV).

Lunkenheimer *et al.*²¹ proposed use of oscillating pumps for HFOV. This reciprocating process produces both active inspiration and expiration processes, eliminating gas entrainment and decompression of gas jets in the conducting airways. With active expiration, the lung volume can be controlled to avoid over-extension of the lung tissue, reducing the risks of lung injuries. HFOV has been used extensively both on neonates²⁵ and adults.^{2,6,27,28} HFV has attracted much research interest; a comprehensive review of this area of study can be found in Chang.³ Fluid dynamics studies include Tanaka *et al.*³⁴ who used laser Doppler anemometer (LDA) to examine the secondary flow intensities and its influence on gas mixing in HFOV in a 3-generation Horsfield¹³ model. Lieber and Zhao¹⁷ also applied LDA to interrogate oscillatory flow in a symmetric single-bifurcation tube model, and found that the flow exhibits quasi-steady behaviors for only about 50% of the oscillatory cycle. Zhang and Kleinstreuer⁴⁴ used a finite-volume code (CFX4.3) to study oscillatory flow in a symmetric triple-bifurcation tube model representing generations 3 to 6 of the human airways under normal breathing and high-frequency ventilation. They found that the oscillatory inspiratory flow is quite different from the equivalent steady-state case even at peak flow. Adler and Brücker¹ studied high-frequency oscillatory flow using particle image velocimetry (PIV) in a 6 generation airway model, and observed mass exchange between child branches at end inspiration or expiration known as Pendelluft. Nagels and Cater²⁹ used large-eddy simulation (CFX 11.0) to study high-frequency oscillatory flow in a 2 generation asymmetric tube model. They observed reverse flow near the walls when the driving velocity is small. Heraty *et al.*¹¹ carried out PIV experiments to measure velocity fields and secondary flows in both idealized and realistic single airway bifurcations under HFOV conditions. They observed the coaxial counter-flow feature, which the flow in the core region of the airway lumen lags behind the flow in the near-wall peripheral region at flow reversal during change of the respiratory phase. They reported that the counter-flow feature persisted for a significant time period. The coaxial counter flow at flow reversal is characteristic of the Womersley solution noted in the classic high-frequency oscillatory straight pipe flow.⁴⁰ This flow feature, however, is neither evident nor reported in Tanaka *et al.*³⁴ It suggests that airway geometry (morphological structure) may also play a role in determining flow characteristics (in association with lung function, e.g. gas transport and mixing for ventilation) under HFOV conditions.

This leads to the current work which aims to provide insight into the structure-function (geometry-flow) relationship of the human lung under different flow conditions using CFD; in particular, to understand the coaxial counter-flow feature in HFOV and quantify the efficiency of convective mixing under different flow conditions. From a kinematical point of view, fluid mixing involves stretching and folding of material lines, and is determined by the fluid velocity field.^{23,30-32} Mixing of this viewpoint is referred to as convective^{5,12} or kinematic¹⁰ mixing. We consider three geometries with increasing complexity: a straight tube, a symmetric single-bifurcation tube system, and a CT-based airway model including

the upper airways and the intra-thoracic airways of up to 7 generations. For the complete airway model, three flow conditions are considered to examine the effects of unsteadiness (oscillation) and convection (inertia). Mixing efficiencies are quantified by the stretch rate analysis.^{23,30,31,32} The paper is laid out as follows. The mathematical formulations for the CFD analysis and the stretch rate analysis are described in the Methods section. In the Results section, oscillatory flows in a straight tube and a single bifurcation are first presented to demonstrate the features of coaxial counter flow and secondary flows. The stretch rates are used to quantify convective mixing in both cases. We then compare the characteristics of flows under three flow conditions in the complete airway model and quantify their stretch rates at the end of cycles and in the vicinity of flow reversal. In the Discussion section, the counter-flow features and mixing efficiencies are discussed in conjunction with existing literatures. Concluding remarks are drawn in the last section.

Methods

Fluid solver

The airflow is simulated using large-eddy simulation (LES) which solves the filtered continuity and momentum equations (1) and (2) for incompressible flow.

$$\frac{\partial u_i}{\partial x_i} = 0 \quad (1)$$

$$\frac{\partial u_i}{\partial t} + u_j \frac{\partial u_i}{\partial x_j} = - \frac{i}{\rho} \frac{\partial p}{\partial x_i} + (v + v_T) \frac{\partial^2 u_i}{\partial x_j \partial x_j} \quad (2)$$

where u_i is the velocity component in the i direction, p is the pressure, ρ is the fluid density, $\nu (= \mu/\rho, \mu$ is the dynamic viscosity) is the kinematic viscosity, and ν_T is the subgrid-scale (SGS) eddy viscosity. The air properties of $\rho = 1.2 \text{ kg/m}^3$ and $\nu = 1.7 \times 10^{-5} \text{ m}^2/\text{s}$ are adopted. Hereafter (x_1, x_2, x_3) and (x, y, z) are interchangeable, so are (u_1, u_2, u_3) and (u, v, w) .

The fractional four-step method is applied to solve equations (1) and (2). The continuity equation is enforced by solving a pressure-Poisson equation. The implicit characteristic-Galerkin approximation together with the fractional four-step algorithm is employed to discretize the governing equations, being of second-order accuracy in time and space.¹⁸ The SGS model of Vreman³⁹ is adopted for calculation of the eddy viscosity ν_T to capture both turbulent and transitional flows. The solver has been validated for flows under various conditions.^{4,16,19,41} A validation case against LDV measurements will be presented later.

CT image based central airway model and 1D centerline model

The three-dimensional (3D) human airway model shown in Fig. 1a was reconstructed from CT images for realistic representation of the human upper airway and tracheobronchial tree. The model is composed of upper airways and up to 7 generations of intra-thoracic airways.^{4,19,20} The trachea is counted as generation 0. There are a total of 70 small peripheral bronchi in this airway geometry. The distributions of the child-branch angle (the angle between two child branches) and the ratio of child-branch diameter over parent-branch diameter are displayed in Figs. 1b and 1c by generation. The major (minor) diameter is that of the child branch having the larger (smaller) diameter. The average child-branch angle is 85° and the average over generations 3-5 is 67° , which is in good agreement with Horsfield.

¹³ The average diameter ratio (including both major and minor diameters) is 0.75, agreeing well with Majumdar *et al.*²⁴ Beyond these CT-resolved airways, the conducting airway tree is supplemented with a physiologically-consistent 1D centerline airway model. The 1D centerline model is generated by the volume filling method.^{35,36} The resulting 1D model has 25 generations and is specific to the geometry of the subject's lung. The changes in lobar volumes are determined by two sets of CT images measured at two lung volumes. The volume changes are then used to determine lobar ventilations and the flow rates at the 1D terminal bronchioles. The flow rates at the 3D peripheral airways are obtained by the connectivity of the 1D tree and mass conservation.^{20,42,43} Variants of 3D-1D and 3D-impedance coupled approaches have previously been applied to air flow in the human respiratory system²² and blood flow in the human arterial system.^{8,9,38}

Breathing conditions for the CT-based airway model

A sinusoidal flow waveform with a parabolic velocity profile is imposed at the mouth-piece inlet of the CT-based airway model as the breathing waveform. For the HFOV case, the simulation is performed with a tidal volume (V_T) of 47 ml and a breathing frequency of 377 breaths per minute ($f = 6.28$ Hz), which fall in the typical range of HFOV. For comparison purpose, two other cases using the same model are computed. One case represents a normal breathing case (denoted by NORM) with $V_T = 500$ ml and a breathing frequency of 12.5 breaths per minute ($f = 0.2$ Hz). The second case is a clinically-impractical case with $V_T = 16.58$ ml and $f = 6.28$ Hz, which yields the same oscillatory frequency as HFOV and the same peak Reynolds number (Re) as NORM, thus being denoted as a high-frequency normal- Re case (HFNR). It is noted that HFNR and NORM have the same minute ventilation. The three cases allow examination of the respective effects of unsteadiness and convection. The flow parameters for these cases are summarized in Table 1. Time step sizes of $t = 2.0 \times 10^{-5}$, 1.0×10^{-5} , and 5.0×10^{-6} s are used for NORM, HFNR, and HFOV, respectively, to satisfy the Courant-Friedrichs-Lewy (CFL) condition.

The CFD mesh for the CT-based airway model consists of 899,465 points and 4,644,447 tetrahedral elements. We tested a series of consecutively finer meshes of **I**) 1,305,429 elements, **II**) 2,573,085 and **III**) 4,644,447 tetrahedral elements. The kinetic energies based on the radial velocity component of the secondary flow at station C in Fig. 1a in the trachea are compared for these meshes at peak inspiration. The differences of secondary flow energies between meshes **I**) and **II**) is 8.3% and it is 2.4% between meshes **II**) and **III**), indicating the results are mesh-insensitive. The mesh **III**) is chosen for study.

Stretch rate analysis

The stretch rate³⁰ was adopted by Roberts³¹, Roberts and Mackley³², and Mackley and Neves Saraiva²³ to quantify the extent of convective mixing, which is the non-diffusive component of the mixing mechanism. A higher stretch rate indicates higher mixing efficiency. Massless particles accompanied by three line elements, which are initially oriented in the respective x, y, and z directions $(1,0,0)^T$, $(0,1,0)^T$ and $(0,0,1)^T$, are tracked in a Lagrangian framework. For each particle, the three corresponding line elements are deformed and stretched kinematically by local velocity gradients as described below.

$$\frac{Dm_i}{Dt} = m_j \frac{\partial u_i}{\partial x_j} - m_i (m_j S_{jk} m_k) \quad (3)$$

$$S_I(t) = \frac{D(\ln\lambda)}{Dt} = m_j S_{jk} m_k \quad (4)$$

$$S_T(t) = \frac{1}{t} \int_0^t \left(\frac{D\ln\lambda}{D\tau} \right) d\tau \quad (5)$$

where m_i is the orientation vector of a line element and $m_i m_i = 1$, u_i is the velocity component i , $S_{ij} = (\partial u_i / \partial x_j + \partial u_j / \partial x_i) / 2$ is the symmetric stretching tensor, λ is the specific rate of stretching, and s_I is the instantaneous stretch rate, also known as the stretching function. The time-averaged stretch rate s_T is calculated from the instantaneous stretch rate as above. Both instantaneous and time-averaged stretch rates have a dimension of s^{-1} . The stretch rates s_I and s_T computed by Eqs. (4) and (5) are for one particle released at a specific location. The stretch rate presented later is the ensemble average based on a number of particles being released at different locations unless otherwise noted. If an oscillatory flow behaves in a kinematically reversible fashion, the time-averaged stretch rate at end cycle is zero.

Flow regimes

To study the characteristics of oscillatory secondary flow in a tubal branching network, it is important to know about the expected flow features in terms of key dimensionless parameters. Jan *et al.*¹⁴ categorized the oscillatory flow in a model bifurcation into three regimes according to two dimensionless parameters. One parameter is the dimensionless frequency α^2 , where $\alpha = a \sqrt{\omega} / v$ is the Womersley parameter. $\omega = 2\pi / T = 2\pi f$ (T , period in s; f , frequency in Hz) is the angular frequency and a is the average radius of an airway segment (or a tube). The other parameter is the local dimensionless stroke length L / a , where $L = v_t / A$ (v_t is the local tidal volume, and $A = \pi a^2$ is the average cross-sectional area of an airway segment). The Reynolds number is given by $Re = \alpha^2 (L / a)$ if the breathing waveform is a sinusoidal function.

Figure 2 shows the demarcation of three flow regimes: I) unsteady flow; II) viscous flow, and; III) convective flow, defined by Jan *et al.*¹⁴, according to the values of α^2 and L / a . The convective regime III is further subdivided into IIIa and IIIb based on the extent of unsteadiness of the flow. Because $Re = \alpha^2 (L / a)$, the constant Re on a logarithmic scale corresponds to a line with a negative slope. For example, the bold solid line for $Re = 30$ separates the viscous and convective regimes, whereas the line for 1,500 separates the convective and turbulent regimes. The two dashed lines mark $Re = 100$ and 740. In the unsteady regime the flow is characterized by the Womersley solution, whereas in the viscous regime it behaves like Poiseuille flow. Both Womersley and Poiseuille solutions are linear solutions, in which the effects of convective inertia are negligible, in contrast to the convective regime. The flow parameters for each of the airway segments in the 3D CT-based airway model are marked in the figure for the cases of NORM (squares), HFOV (circles), and HFNR (triangles). For NORM, the dimensionless frequency α^2 falls in the range between 0.12 and 7, and the stroke length L / a ranges from 133 to 1,353. For HFOV, α^2 is between 3.6 and 210, and L / a is between 12 and 127. Since HFNR has the same frequency as HFOV and the same peak Re as NORM, HFNR has the same range of α^2 as HFOV but is bounded by $Re = 1,500$ as NORM. The maximum Re at the trachea for NORM is 1,288, and it is 3,656 for HFOV. All of the segmental Re for NORM and HFNR are below 1,500, whereas six segments for HFOV exceed 1,500.

Also exhibited in Fig. 2 are the conditions computed with the 1D centerline model using the parameters averaged by generation for the three cases (open symbols). Each open symbol represents the average flow condition for each generation of the entire airway tree beginning from the trachea to terminal bronchioles (distributing from right to left in the figure). For HFOV, the distribution curve is shifted downwards to the right and the effects of convection penetrate deeper into the lungs (note that the curve intersects $Re = 30$ at the 7th generation in both NORM and HFNR, but at the 9th generation in HFOV). Overall, the characteristics of HFOV are more turbulent in the central airways and more convective in the smaller airways. For HFNR, due to its smallest L/a and high α^2 , the flow in the range of $\alpha^2 > 10$ (denoted by “IIIb-CONVECTIVE” in Fig. 2) may behave more similarly to the Womersley solution.

To investigate the effects of unsteadiness (oscillation) versus convection (inertia), the flow parameters at point A ($Re = 100$, $\alpha = 7.0$) in Fig. 2 in the unsteady regime I and point B ($Re = 740$, $\alpha = 7.0$) in the convective regime IIIb (more unsteadiness) are chosen for simulations of the flow in a straight tube and the flow in a symmetric bifurcating tube. The bifurcating tube model of Zhao and Lieber⁴⁵ and Lieber and Zhao¹⁷ shown in Fig. 3a is adopted for two purposes. One purpose is for model validation by comparing with the data measured with LDA for oscillatory flow in the bifurcating tube model.¹⁷ Their flow condition has a peak $Re = 2,077$ and $\alpha = 4.3$, corresponding to point C in Fig. 2. The second purpose is to investigate the differences between flow structures in regimes I and IIIb, and the deviation of the flow behavior from the Womersley solution. Use of a symmetric bifurcating tube facilitates comparison with the straight tube case. The effects of airway geometry and turbulence (which can only be captured in the CT-based airway model) will be examined by comparing the flow structures at bifurcations between generations 2 and 3 (G2-3) and 3 and 4 (G3-4) at three breathing conditions of NORM, HFOV, and HFNR. The local flow parameters at the parent branches of the G2-3 and G3-4 bifurcations are marked by the color-coded boxed 2 and 3 in Fig. 2, respectively.

Results

Model validation

The dimension of the symmetric bifurcating tube model is illustrated in Fig. 3a. The formula used to generate the model and stations 2, 4, 10, and 15 are given in Zhao and Lieber.⁴⁵ An enlarged view of the model is shown in Fig. 3b, where station S12.5 is located midway between stations S10 and S15. The child-branch angle of 70° falls within the range of those at generations 3 and 4 (see Fig. 1b). The diameter ratio between child and parent branches is $1/\sqrt{2} \approx 0.7$, which also agrees with the current CT data (Fig. 1c). A sinusoidal flow waveform with the Womersley velocity profile is imposed at the boundary face of the parent branch. The mesh consists of 141,403 nodal points and 747,344 tetrahedral elements. The fluid properties and flow conditions used by Lieber and Zhao¹⁷ are adopted. The instantaneous velocity profiles (solid lines) at stations S2, S10, and S15 at $t/T = 0.2$ (inspiration) and 0.7 (expiration) in the bifurcation and transverse planes are plotted against the measurement data (solid squares) of Lieber and Zhao.¹⁷ The bifurcation plane is coplanar with the centerlines of the three branches, whereas the transverse plane for each of the three branches is perpendicular to the bifurcation plane and coplanar with the centerline of an individual branch. Overall, they are in good agreement. It is noted that the CFD solution is more symmetric with respect to $r/R = 0$ than the measurement data. For instance, in the range of $r/R < 0$ in Fig. 3f, the current data over-predict (under-predict) the experimental data at S2 (S15), but they agree with the CFD data of Zhang and Kleinstreuer.⁴⁴

Womersley solution and flow in a straight tube

The straight tube used in the simulation is a 3D tube with radius $a = 4.6$ mm and length of $10a$. The mesh for the tube consists of 82,144 nodal points and 453,586 tetrahedral elements. Considering a single harmonic case in a straight tube of radius a , we impose the Womersley axial velocity (u_a) profile⁴⁰ at the inlet.

$$u_a(r, t) = \frac{A_o}{\rho} \frac{1}{i\omega} \left\{ 1 - \frac{J_o(\alpha r i^{3/2})}{J_o(\alpha i^{3/2})} \right\} e^{i\omega t} \quad (6)$$

where A_o is the amplitude of pulsation, ω (the angular frequency) and α (the Womersley parameter) are previously defined, r is the normalized radial position (with $r = 0$ at the centerline of the tube, and $r = \pm 1$ at the wall), i is the imaginary unit, and J_k is the k -th order complex Bessel function of the first kind. With a given Re (or the maximum Re for a

pulsatile flow), the mean velocity U is calculated using $Re = \frac{U(2a)}{\nu}$, where U is the sectional average velocity at peak inspiration. Then the maximum flow rate Q_{max} is computed by $Q_{max} = U\pi a^2$, and A_o can be determined from

$$Q = \frac{\pi a^2 A_o}{\rho} \frac{1}{i\omega} \left\{ 1 - \frac{2 J_1(\alpha i^{3/2})}{i^{3/2} \alpha J_o(\alpha i^{3/2})} \right\} e^{i\omega t} \quad (7)$$

Because the axial velocity u_a in equation (6) and the flow rate Q in equation (7) are complex numbers, the real parts of equations (6) and (7) are taken in the calculation. The time in equations (6) and (7) is offset to keep Q in phase with the imposed sinusoidal flow waveform so that $Q = 0$ at $t/T = 0, 0.5$ and 1 .

Figure 4 presents the results of the flow in a straight tube with the flow parameters of $Re = 100$ and $\alpha = 7$, at point A marked in Fig. 2. The Womersley velocity profiles yielded from equation (6) at selected time points during a sinusoidal cycle are displayed in Fig. 4a. It is noted that the Womersley profiles do not vary along the axial direction of a straight pipe. The flow rates at $t/T = 0, 0.5$ and 1 are zero. The inspiratory and expiratory phases occur during $0 \leq t/T \leq 0.5$ and $0.5 \leq t/T \leq 1$, respectively. Coaxial counter flow (co-existence of positive and negative axial velocities due to phase lag between core and peripheral flows) is observed in the vicinity of $t/T = 0, 0.5$, and 1 when flow reversal takes place at end inspiration and end expiration. It is worth noting that the velocity profile is not symmetric in time with respect to $t/T = 0.5$ and 1 . For example, the profile at $t/T = 0.375$ differs from that at $t/T = 0.625$ although they have the same time distances from $t/T = 0.5$. This is because the flow changes phase faster in the peripheral region than the core region. Nevertheless, the profiles at t/T are the mirror images of those at $t/T + 0.5$ (same shape but opposite sign), cf. those at dimensionless times of 0.125 and 0.625 . As a result, a Lagrangian particle released in any location of the tube experiences zero net displacement at the end of a cycle. The profiles at peak inspiration ($t/T = 0.25$) and expiration ($t/T = 0.75$) are blunt. An increase in frequency makes the velocity profile blunter and the peripheral counter flow narrower as displayed in Fig. 4b, but the period-normalized time duration when counter flow exists remains essentially unchanged. The Womersley velocity profiles with the flow parameters at A are imposed as the flow boundary condition at the left-hand-side boundary face of the straight tube. A pressure boundary condition is imposed at its right-hand-side boundary face. The simulated velocity profiles at various stations along the tube remain the same as the

Womersley solution imposed at the boundary face, and are plotted against the Womersley solution at various times in Fig. 4c. The agreement between them is good, confirming that the flow condition at point A in a straight tube yields the Womersley solution.

With the imposition of the flow condition at point B which has the same frequency as A, but a higher Re than A, the CFD-simulated velocity profiles at various times during a cycle (not shown) exhibit the same shapes as those of Fig. 4c, but have different magnitudes. This is in agreement with the Womersley solution equation (6) that the shape of velocity profile depends on frequency (cf. Figs. 4a and 4b), with a given frequency an increase in velocity amplitude increases Re . Thus, in spite of an increase in Re for point B which places it in the convective IIIb regime, the straight and axisymmetric features of the tube constrain the flow motion only in the axial direction. As a result, the convective terms in the Navier-Stokes equations are zero, yielding the linear Womersley solution.

Flow in a bifurcating tube model

The radius of the parent branch in the single-bifurcation tube model is rescaled to that of the straight tube in order to use the same flow parameters as in the straight-tube case. The Womersley profile is imposed at the parent-branch boundary face of the model (Fig. 3a) to examine the effects of bifurcation on flow structures. Unlike the straight-tube case, the curvature at the bifurcation may induce secondary flow motions in the radial direction due to inertia. The flow conditions at point A ($\alpha = 7$, $Re = 100$) and point B ($\alpha = 7$, $Re = 740$) in Fig. 2 are examined. For the case of $Re = 100$ ($Re = 740$), Fig. 5 (Fig. 6) shows the color-coded velocity vectors in the bifurcation plane at flow reversal during end expiration and early inspiration in Figs. 5a-d (Figs. 6a-d) and during end inspiration and early expiration in Figs. 5e-h (Figs. 6e-h). The red (blue) color denotes positive (negative) axial velocity, flowing to the right (left) side. Coaxial counter flow exists over a longer time period before flow reversal than after reversal. This is why counter flow is observed at $t/T = 0.94$ and 0.44 , but not at $t/T = 1.06$ and 0.56 . This is true for both Re cases (see Figs. 5 and 6). At $Re = 100$ (Fig. 5), in spite of the presence of the bifurcation, the counter-flow feature is evident and not distinguishably perturbed in both parent and child branches, resembling the imposed Womersley profile. However, at $Re = 740$ Fig. 6 shows significant deviation from the Womersley profile, especially near the bifurcation. At end expiration in Figs. 6a and 6b, the flow coming off the child branches has relatively high inertia and appears to detach from the wall of the parent branch at the bifurcation due to bifurcation curvature. A similar effect is observed at end inspiration, but the major deviation is found in the child branch due to change of the axial flow direction. These deviations are amplified after flow reversal at $t/T = 1.03$ on inspiration and $t/T = 0.53$ on expiration. The counter-flow feature appears to be absent in some regions of the parent branch at $t/T = 1.03$ (red only) and the child branches at $t/T = 0.53$ (blue only).

To better understand the flow characteristics, Fig. 7 shows the enlarged view of the flow near the bifurcation in the bifurcation plane and the cross-sectional velocity vectors at stations S4 and S12.5, whose location and numbering scheme are based on the formula of Zhao and Lieber.⁴⁵ Figures 7a and 7b (7e and 7f) are at end expiration $t/T = 0.97$ and early inspiration $t/T = 1.03$, respectively, for $Re = 100$ (740). And Figs. 7c and 7d (7g and 7h) correspond to end inspiration $t/T = 0.47$ and early expiration $t/T = 0.53$, respectively, for $Re = 100$ (740). The velocity magnitude is much smaller at $Re = 100$ than at $Re = 740$, and the secondary flow velocity is weaker than the axial velocity. Therefore, the velocity vector length in the bifurcation plane at $Re = 100$ is magnified by 7.4 times than that of $Re = 740$, and the vector length at S4 and S12.5 is amplified by 4 times than those in the bifurcation plane for clarity. Counter-rotating vortices are observed at S4 and S12.5 although they are very weak at $Re = 100$. These secondary flow structures are Dean vortices found in a curved pipe flow.³³ In the bifurcation plane of the $Re = 100$ case, the flow at $t/T = 0.97$ (1.03) is

almost the reverse (opposite sign) of that at $t/T = 0.47$ (0.53). This is because the Womersley profiles at t/T are the mirror images (same magnitude, but of opposite sign) of those at $t/T + 0.5$ as shown in Fig. 4a. However, this is not true for the flow feature in the radial direction. For example, at S12.5 despite the change of phase in the axial flow, the counter-rotating vortices at $t/T = 0.97$ and 0.47 (1.03 and 0.53) rotate in the same directions. This is because the rotational direction of the vortices is dependent on the curvature of the tube, rather than the direction of the axial flow. With increasing Re to 740, the secondary flow vortices are intensified. At end expiration at $t/T = 0.97$ (Fig. 7e), two pairs of counter-rotating vortices at S4 in the parent branch appear to wash away the counter flow (red) in the peripheral region toward the bifurcation plane. Likewise, a pair of counter-rotating vortices at S12.5 in the child branch at end inspiration $t/T = 0.47$ (Fig. 7g) appear to wash away the counter flow (blue) in the peripheral region toward the upper side of the branch. After flow reversal at $t/T = 1.03$ (Fig. 7f) and 0.53 (Fig. 7h), the axial flow directions are reversed but the secondary flow characteristics remain qualitatively the same. Unlike $Re = 100$, the flow structures at $Re = 740$ in the bifurcation plane at $t/T = 0.97$ and 0.47 (1.03 and 0.53) no longer differ merely by the axial flow direction because primary secondary vortices are formed after bifurcation in the downstream flow, e.g. in the parent branch at end expiration (see S4 in Figs. 7e and 7f) and in the child branch at end inspiration (see S12.5 in Figs. 7g and 7h).

Flow in the CT-based airway model

In this section, we compare the CT-based airway cases under three different breathing conditions. They are the normal breathing case (NORM), the high-frequency normal- Re case (HFNR), and the high-frequency oscillatory ventilation case (HFOV). The distributions of their corresponding dimensionless frequency α^2 , dimensionless stroke length La , and Re are exhibited in Fig. 2 (see also Table 1). HFNR is much closer to the unsteady regime than the other two cases, and its dimensionless stroke length is close to 7, which is also the average ratio of airway segment length over radius. At peak flow rate, the Re of HFOV in the trachea is about 3 times greater than those of NORM and HFNR. Thus, the peak speed of the turbulent laryngeal jet in HFOV is also about 3 times greater than the other two cases. At end expiration and early inspiration at $t/T = 0.97$ and 1.03 (end inspiration and early expiration at $t/T = 0.47$ and 0.53), the color-coded velocity vectors in a vertical plane for the three cases are compared in the left (right) two panels of Fig. 8. The vertical plane is coplanar with the trachea and the left and right main bronchi. The downward (upward) vertical velocity is marked with the red (blue) color. Fig. 8a shows that counter flow at flow reversal is absent in NORM. For HFNR, the flow condition at the trachea has about twice higher Womersley parameter α than A and B (see Fig. 2), and an La value between A and B, and a higher peak Re of 1,288 than B with $Re = 740$. As compared with the flow structures in the single-bifurcation model displayed at $t/T = 0.97$ in Fig. 5b ($Re = 100$, point A) and Fig. 6b ($Re = 740$, point B), the counter-flow feature seems to be present, but is irregular due in part to the complex geometry of the realistic airway model and the higher Re of the flow, which can yield flow separation and recirculation. At early inspiration $t/T = 1.03$, the inspiratory flow (red) covers a greater extent with the remnant expiratory flow (blue) embedded in the core region of the trachea and the left and right main bronchi. This feature resembles those shown in Figs. 5c and 6c, but exhibiting a patchy appearance. At end inspiration $t/T = 0.47$, the counter-flow feature is also observed. The blue region formed at the outer wall of the bifurcation due to inertia is similar to that of the single-bifurcation case shown in Fig. 6f. Similarly, at early expiration $t/T = 0.53$, the remnant inspiratory flow (red) is observed as in Fig. 6g, but also has a patchy appearance. For HFOV, due to higher Re the flow is characterized by small-scale eddy motions. For example, at end expiration $t/T = 0.97$ the inspiratory flow (red) near the bifurcation, which is ahead of the phase, is found in smaller regions than HFNR. This feature is also observed at end inspiration $t/T = 0.47$. Furthermore, the patches representing the remnant flow in HFNR at early inspiration $t/T = 1.03$ and early

expiration $t/T = 0.53$ appear to break up into small pieces, obscuring the counter-flow feature if any.

Next we shall examine the flow structures at the bifurcation between generations 2 and 3. The bifurcation located in the dot-dashed box in Fig. 1a is examined. The flow parameters of the parent branch of the bifurcation for the three cases are marked as boxed 2 in Fig. 2 with their respective colors (see also Table 2). The flow condition for NORM is in the convective regime IIIa, being far away from the unsteady regime. The dimensionless frequencies α^2 for HFOV and HFNR are very close to those of A and B used for the bifurcating tube model. HFNR is closer to the unsteady regime I, whereas HFOV almost overlaps with B in Fig. 2. The major differences between the CT-based-airway case and the single-bifurcation case are two-fold. First, the geometric feature of the CT-based model is more complicated, but realistic, as compared with the tubal model. Second, the upstream and downstream flow structures entering the CT-based bifurcation are computed in a whole airway setting that minimizes the effects of boundary conditions. Figure 9 shows the flow structures in a bifurcation plane at end expiration and early inspiration $t/T = 0.97$ and 1.03. Using the single-bifurcation case (Figs. 6b and 6c) as a reference, Figs. 9a and 9b for NORM do not reveal any counter-flow feature. For HFNR, the counter-flow feature is observed. The expiratory fluid stream (blue) at $t/T = 0.97$ in Fig. 9c is particularly clear, resembling Fig. 6b. At early inspiration (Fig. 9d), the remnant expiratory flow is diminishing, primarily remaining in the core region of the branches. For HFOV, the counter-flow feature is not discernible as exhibited in Figs. 9e and 9f, although its flow parameters are essentially the same as at B. The above features at $t/T = 0.97$ and 1.03 for the three cases are also observed at end inspiration and early expiration $t/T = 0.47$ and 0.53. Figures 10a and 10b, for example, show that the flow conditions for NORM do not produce counter flow. For HFNR, the counter-flow feature is particularly evident in the child branches as shown in Figs. 10c and 10d (cf. Figs. 6f and 6g), despite the presence of small vortices in the parent branch. For HFOV, Figs. 10e and 10f show that the flow is more disorganized, comprising several vortices so that the counter-flow feature is not discernible.

Lastly, we examine the flow structures at the bifurcation between generations 3 and 4. The bifurcation in the dashed box in Fig. 1a is investigated. The flow parameters of the parent branch of the bifurcation are marked as boxed 3 in Fig. 2 (see also Table 2). For NORM, it is in the convective regime IIIa. For HFOV and HFNR, their dimensionless frequencies fall on the dashed line that is extended from the demarcation line between the unsteady and viscous regimes. The dashed line further classifies the convective regime into two sub-regimes IIIa (quasi-steady) and IIIb (unsteady). Figure 11 shows the flow structures for the three cases at end expiration and early inspiration. The counter-flow feature is completely absent in NORM and HFOV, and is either nearly diminishing or absent in HFNR. Similarly, at end inspiration and early expiration the counter-flow feature is not observed in these cases (not shown).

Stretch rate analysis

For illustration of the correlation between flow structures and stretch rates, we first consider the time history of the stretching and orientation of a passive line tracer consisting of uniformly distributed passive Lagrangian particles in the straight-tube case at $Re = 740$ that yields the Womersley solution. The particles are initially aligned along a line in the radial direction below the interface between two opposing flows at flow reversal as denoted by red (number 1) in Fig. 12a. Figure 12a shows the locations and shapes of the tracer at $t/T = 0, 0.25, 0.6,$ and 0.75 , corresponding to beginning inspiration, peak inspiration, early expiration and peak expiration, respectively. The Womersley velocity profiles at these times are also exhibited to show the corresponding local velocity gradient. At inspiration, the tracer is stretched, yielding a positive slope by the positive velocity gradient of the flow. At early

expiration $t/T = 0.6$, the flow creates an L-shaped tracer with a negative-slope upper part and a positive-slope lower part. At peak expiration, the slope of the tracer becomes negative. At the end of one cycle, the tracer returns to its original location due to the reversible kinematics of the linear Womersley solution shown in Fig. 4a.

Next, we apply the stretch rate analysis to a particle released in the middle of the above tracer. The time histories of the three orientation components m_i of a line element calculated by Eq. (3) are shown in Fig. 12b. The initial vector $(m_1, m_2, m_3) = (0, 1, 0)$ is in parallel to the radial direction of the tube. As time progresses, m_3 remains unchanged in the absence of shear. The line element experiences rotation with increasing m_1 and decreasing m_2 due to positive shear of the flow before reaching peak inspiration at $t/T = 0.25$ as in Fig. 12a. At expiration $t/T = 0.6$, the orientation of the line element is first reversed back to $(0, 1, 0)$, and then m_1 is changed to -1 due to negative shear in response to the change of flow direction. At the end of one cycle, the line element recovers its initial orientation. In one cycle the line element experiences stretching in opposite directions and is restored to its initial orientation twice. The instantaneous (s_T) and time-averaged (s_T) stretch rates for this line element are displayed in Fig. 12c, and the enlarged view of s_T is plotted in Fig. 12b. The time history of the instantaneous stretch rate shows alternating positive and negative stretches twice, corresponding to the twice-stretched tracer illustrated above. As a result, at the end of one cycle, the time-averaged stretch rate s_T is zero, e.g. $t/T = 1$ and 2 , signifying a reversible process. The relatively high s_T at initial time is due to small time t in the denominator of Eq. (5). The stretch rate analysis shows that there is no net convective mixing at the end of one cycle in spite of the existence of counter flow and phase lag in the straight-tube system that sustains the Womersley solution.

For the single-bifurcation cases shown in Figs. 5 and 6 for $Re = 100$ and 740 , about 1,700 particles are released in the parent branch at a distance of $0.88D$ and $6.5D$ from the bifurcation for $Re = 100$ and 740 , respectively. The ratio of the particle release distances for $Re = 100$ and 740 is the ratio of the stroke lengths for the two cases so that the spreads of particles with respect to the bifurcation for both cases are dynamically similar. Application of the stretch rate analysis to two cycles of data yields the maximum-instantaneous and time-averaged stretch rates of 13.2 and 1.49 (29.2 and 10.9) s^{-1} , respectively, for $Re = 100$ (740). The stretch rates are no longer zero due to the formation of secondary vortical motions. The ratio of the time-averaged stretch rates for both cases is close to the ratio of Re .

For the whole airway cases of HFOV and HFNR, the stretch rates based on about 1,700 particles are presented. The particle release distances of $5.27D$ and $1.86D$ relative to the carina are marked by A and B in Fig. 1a for HFOV and HFNR, respectively. The ratio of the release distances is the same as the ratio of the stroke lengths for dynamic similarity of particles reaching the carina. The NORM case is not compared here because it has a much longer dimensionless stroke length (e.g. 184 in the trachea) than HFOV and HFNR (17.3 and 6.1 in the trachea) so that the majority of particles released in NORM would be advected out of the model by the end of a cycle, making the comparison difficult if not impossible. Figure 13 shows the instantaneous and time-averaged stretch rates for HFOV and HFNR. The instantaneous stretch rates have local minima near flow reversal at $t/T \sim 0.5, 1, 1.5$ and 2.0 for both cases, suggesting that the flow structures at flow reversal are less effective in mixing as compared with those at higher flow rates. The time-averaged stretch rates s_T at the end of two cycles are 24.5 and $81.4 s^{-1}$ for HFNR and HFOV, respectively. The s_T ratio between HFOV and HFNR is 3.3 , which is slightly greater than the Re ratio of 2.8 . It is noted that $\sim 50\%$ of particles released in HFOV are advected out of the airway model as compared with $\sim 5\%$ in HFNR. The $\sim 1,700$ particles used in calculation of the above stretch rates are those remaining active inside the airway models after two breathing cycles. The number of active particles drops with time. Those being advected out of the model tend to

experience higher stretch rates because of their association with high-speed fluid stream (thus reaching the exits faster). By using active particles at any time instant to compute the stretch rates in HFOV (HFNR), we obtain the thin lines in Fig. 13b, yielding a time-averaged stretch rate of $107 (24.6) \text{ s}^{-1}$. The s_T ratio becomes 4.3.

According to the Womersley solution and the single-bifurcation case, the counter-flow phenomenon is most evident between ± 0.06 around $t/T = 0.5$ and 1. With the short time duration of $0.12t/T$ centered on end expiration and inspiration, we can quantify the contribution of flow structures at flow reversal, such as secondary vortices and counter flow, to mixing under different frequencies and Re along with the influence of the turbulent laryngeal jet flow for the cases of NORM, HFNR, and HFOV. About 2,000 particles are released initially in the solid box surrounding the carina in Fig. 1a. The particle release site is selected by taking into consideration the long stroke length of NORM. The instantaneous and time-averaged stretch rates for these cases are displayed in Fig. 14. At end expiration and early inspiration (left panel), the instantaneous stretch rate s_I for NORM behaves quite differently from those of HFNR and HFOV, having a local minimum of nearly zero at around flow reversal $t/T \sim 1$. Inspection of the flow structures in Fig. 8a shows weak flow activities in NORM at $t/T \sim 1$. As a consequence, the time-averaged stretch rate s_T for NORM at $t/T \sim 1$ has a small slope. The instantaneous stretch rates for HFNR and HFOV are not zero, being attributed to the irregular counter-flow structures shown in Figs. 8b and 8c. The oscillatory behavior exhibited in the instantaneous stretch rate s_I of HFOV may be due to the turbulent eddy motions as revealed in Fig. 8c. Overall, at $t/T \sim 1$ the maximum instantaneous stretch rates $s_{I,max}$ for NORM, HFNR, and HFOV are 29, 56 and 145 s^{-1} , respectively, and the time-averaged stretch rates s_T over the period of $0.12t/T$ centered at $t/T=1$ are 0.58, 4.9 and 9.5 s^{-1} , respectively. The $s_{I,max}$ ratio is $\sim 1:1.9:5$, and the s_T ratio is $\sim 1:8.4:16.4$.

Next we shall consider the stretch rates at end inspiration and early expiration $t/T \sim 1.5$. The distributions of the stretch rates for the three cases are qualitatively similar to those at $t/T \sim 1$. Overall, the stretch rates at $t/T \sim 1.5$ are smaller than those at $t/T \sim 1$. The maximum instantaneous stretch rates $s_{I,max}$ for NORM, HFNR, and HFOV are 26, 36 and 138 s^{-1} , respectively, and the time-averaged stretch rates s_T are 0.46, 2.4 and 6.7 s^{-1} , respectively. The $s_{I,max}$ ratio is $\sim 1:1.4:5.3$, and the s_T ratio is $\sim 1:5.2:14.6$. It is noteworthy that in the single-bifurcation model shown in Fig. 7, at end inspiration $t/T \sim 1.5$ a pair of secondary vortices is formed in the child branches, while at end expiration $t/T \sim 1$ two pairs of secondary vortices are formed in the parent branch. More vortices formed at end expiration yield greater stretch rates and more effective convective mixing.

Discussion

Counter Flow

Heraty *et al.*¹¹ investigated the spatial flow structures under high-frequency oscillatory ventilation in both idealized and anatomically-realistic bifurcation models using PIV. One of the important findings of their study was that the inspiratory and expiratory fluid streams co-exist (known as coaxial counter flow) in the airways for significant periods around flow reversal for both idealized and realistic models. Shear layers were formed between the opposing fluid streams, and persisted for slightly longer in the wider left child branch than in the right child branch. Vortical structures were resulted from the roll-up of shear layers in both models. More specifically, in their Fig. 3 with $Re = 740$ and $\alpha = 7$ (the same flow parameters as point B in Fig. 2), counter flow and shear layers were found further away from flow reversal at early inspiration $t/T = 0.057$ and 0.115, at end inspiration $t/T = 0.452$, and at early expiration $t/T = 0.623$.

Contrary to their work, the current single-bifurcation case with the same flow parameters ($Re = 740$ and $\alpha = 7$) shows that these structures are completely absent further away from flow reversal at $t/T = 1.06$ (or 0.06) and $t/T = 0.56$ (see Figs. 6d and 6h). That is, the time period for the existence of counter flow and shear layers around flow reversal reported in Heraty *et al.*¹¹ is about twice longer than that of the current study. To investigate the potential effect of an imposed velocity profile on the counter-flow period, a uniform velocity profile (to mimic the blunt feature of the Womersley velocity profile) with the same sinusoidal flow waveform as before is imposed in the single-bifurcation model. The result shows that the uniform profile rapidly adjusts to the Womersley profile in the parent branch. To investigate the effect of the shape of breathing flow waveform, we impose a triangular waveform that increases the flow rate linearly from zero to the same peak inspiratory flow rate as the sinusoidal waveform, reduces it linearly to zero at end inspiration and then repeats it for the expiratory phase. The triangular waveform has the same frequency as the sinusoidal waveform, but has ~50% lower flow rate at $t/T \sim \pm 0.06$ and ± 0.56 than the sinusoidal one. The result shows that the flow characteristics are qualitatively the same as before, but having a smaller velocity magnitude. Lastly, we design a case with a sinusoidal waveform only for the inspiratory phase. After end inspiration $t/T = 0.5$ when the flow rate is zero, the inlet boundary velocity is set to zero, maintaining a zero flow rate for $t/T > 0.5$. The results show that the counter-flow structures similar to Figs. 6f and 7g persist within the time window of $t/T = 0.5 - 1.0$, but with decaying velocity magnitude and shrinking thickness of the inspiratory flow region. At $t/T = 0.5$, the thickness of the inspiratory flow in the parent branch is approximately constant, similar to the red region in Fig. 7g. With increasing time, the thickness of the red zone at a distance of $\sim 0.5D$ to the bifurcation point shrinks at a rate faster than other regions. At the center point of that location, the velocity magnitudes at $t/T = (0.5, 0.6, 0.7, 0.8, 0.9, 1.0)$ are $(0.47, 0.42, 0.32, 0.19, 0.11, 0.07)$, and the thicknesses normalized by the parent-branch diameter are $(0.65, 0.42, 0.26, 0.21, 0.21, 0.23)$. Thus, the velocity magnitude drops by 32% (85%) from $t/T = 0.5$ to 0.7 (1.0). The pattern of the narrowing inspiratory flow ahead of the bifurcation resembles that shown in Fig. 3 at $t/T = 0.623$ of Heraty *et al.*¹¹ Thus, the “significant” periods around flow reversal reported in their observations can only be reproduced in the current study with a significantly low flow rate over a non-negligible period around flow reversal.

While the flow structures at flow reversal found in the current single-bifurcation model bear some resemblances to those observed by Heraty *et al.*,¹¹ they exhibit differences as well. For example, we do not observe the roll-up of shear layers due to shear instability and the subsequent vortices formed at the interface between opposing fluid streams at flow reversal under the same flow condition of $Re = 740$. The only vortical structures observed in the current single-bifurcation model are the secondary rotational motions, namely Dean vortices, due to centrifugal instability associated with the curvature of the bifurcation^{4,33}. At end expiration $t/T = 0.97$ and early inspiration $t/T = 1.03$ two pairs of strong counter-rotating vortices are formed in the parent branch (see Figs. 7e and 7f), whereas at end inspiration $t/T = 0.47$ and early expiration $t/T = 0.53$ a pair of counter-rotating vortices are formed in the child branch (see Figs. 7g and 7h). The primary difference between these vortices (found at flow reversal) and those found in a typical breathing condition (evident at peak flow rate rather than at flow reversal) is the spiral pattern of the current vortices that exhibit alternating positive and negative axial velocities, as indicated by the blue and red colors in the figure, along the spiral stream-traces of the vortices.

The branching angle and the diameter of the airways shall also affect the counter-flow structures. Heraty *et al.*¹¹ reported the persistence of quasi-axisymmetric counter flow and shear layers to a greater extent of $t/T = 0.115$ at early inspiration and in the “wider” left child branch of the realistic model as shown in their Fig. 3. In contrast, in the current study Fig. 7f shows that at $t/T = 1.03$ (or 0.03) the counter flow exists in the child branch, but is skewed

toward the inner wall of the bifurcation. As illustrated in the straight-tube and single-bifurcation cases, deviation from axisymmetric counter flow to skewed counter flow is due to the inertia effect augmented in the flow through a curved tube. A close inspection of their idealized and realistic single-bifurcation models shows two major geometric differences between them. Both geometries features happen to yield the same effect of sustaining axisymmetric counter flow. The two features are the ratio of child-branch diameter to parent-branch diameter and the angle between the two child branches. In their idealized model the ratio is ~ 0.84 and the angle is $\sim 63^\circ$, whereas in their realistic model the ratio is ~ 0.68 (0.64) for the left (right) child branch and the angle is 44° . In the current single-bifurcation model (Fig. 3a), the ratio is 0.7 and the angle is 70° , which fall within the ranges of the CT-based airways shown in Fig. 1 with an average ratio of 0.75 and an average angle of 70° . Their models have either a large diameter ratio (thus, yielding a smaller Re in the child branch) or a small angle (thus, a smaller curvature). Both reduce the effect of inertia, resulting in more apparent Womersley-like flow features. It is noted that their realistic model is based on a cadaver, while ours is based on in-vivo imaging.

Convective Mixing

Convective mixing is quantified by instantaneous and time-averaged stretch rates. Lagrangian particles act like micro-sensors that are advected along with the flow and measure the degree of stretching by local flow structures. Coaxial counter flow alone (and associate shear layers) does not contribute to convective mixing as demonstrated in Fig. 12 because the Womersley solution is a linear solution such that passive tracers are reversed back to their original states at the end of one cycle or multiple cycles. With the presence of a bifurcation, at low $Re = 100$ coaxial counter flows are observed in both parent and child branches, and secondary vortices are present but weak, contributing little to mixing. Effective mixing takes place at $Re = 740$ in the single-bifurcation model when strong secondary vortices are induced. The flow becomes irreversible in that strong vortices are formed in the “parent” branch at end expiration and early inspiration, whereas they are formed in the “child” branch at end inspiration and early expiration. Unlike the Womersley solution where the velocity profiles at t/T are mirror images of those at $t/T + 0.5$ (Fig. 4a) and thus they are reversible, secondary vortices at t/T are no longer reverse processes of those at $t/T + 0.5$ due to inertia. Besides, regardless of axial flow direction, vortices on inspiration rotate in the same direction as those on expiration, which depends on the curvature of the bifurcation, contributing to irreversibility and mixing as well.

For the CT-based airway model, three breathing conditions are considered. They are the normal breathing case NORM, the high frequency normal Re case HFNR and the high frequency oscillatory ventilation case HFOV. Although HFNR is clinically impractical, it facilitates the investigation of the respective effects of unsteadiness (oscillation) and convection (inertia). Due to the long stroke length in NORM, we first compare the stretch rates for HFNR and HFOV for two cycles and then compare the stretch rates for the three cases in the vicinity of flow reversal. The results show that flow structures at flow reversal are not as effective as those at peak flow rate in mixing, but they contribute non-negligibly ($\sim 20\%$) to the total of time-averaged stretch rates in both HFNR and HFOV cases (based on the division that the flow structures within ± 0.06 around $t/T = 0.5$ and 1 are regarded as counter-flow related structures). A comparison of time-averaged stretch rates at the end of two cycles shows that mixing in HFOV is about 3-4 times more effective than HFNR, which is slightly greater than the ratio of Re for both cases.

Considering the flow structures at flow reversal near the first bifurcation within the time duration of $\pm 0.06t/T$, the stretch rate analysis shows that an increase in frequency by 30 fold increases the peak instantaneous stretch rate (time-averaged stretch rate) by 1.9 (8.4) fold, whereas an increase in Re by 3 fold increases the peak instantaneous stretch rate (time-

averaged stretch rate) by 2.6 (2) fold. Contrary to HFNR and HFOV, the instantaneous stretch rate at flow reversal in NORM is nearly zero and the time-averaged stretch rate is much smaller than HFNR and HFOV. This demonstrates the unsteady features of the high-frequency oscillatory flow at flow reversal that is characterized by the interplay between counter flow, secondary vortices, and turbulence. Nonetheless, according to the flow visualization at small airways (see Fig. 11) and the flow regime (see Fig. 2), these unsteady flow features are only evident and significant in convective mixing up to the bifurcations between the 3rd and 4th generations of the airways.

Conclusions

In this work, high frequency oscillatory flow was studied using CFD in three models with increasing geometrical complexity, including a straight tube, a symmetric single-bifurcation tube model, and a CT-based trachea-bronchial airway model. The focus of the study is placed on the counter-flow phenomenon at flow reversal and its contribution to mixing. While in the straight-tube case the Womersley velocity profiles are produced, in the single-bifurcation case coaxial counter flow is altered by secondary vortices especially at high Re , resulting in convective mixing. It is also found that counter flow can sustain over a significant time period when the flow rate is set to zero. For the CT-based airway case, three flow conditions were considered to examine the effects of unsteadiness and inertia. It is found that in the normal breathing case the flow structures at flow reversal contribute little to mixing, whereas in the high frequency oscillatory ventilation case the interplay between counter flow, secondary vortices and turbulence enhances mixing at flow reversal.

Acknowledgments

This work was supported in part by NIH grants R01-HL094315, R01-HL064368, R01-EB005823, and S10-RR022421. The authors are grateful to Youbing Yin and Haribalan Kumar for generating meshes and CT images of the airway model and assisting with stretch rate analysis. We thank Drs. C. Kleinstreuer and Z. Zhang for assisting with generation of a single-bifurcation geometrical model. We also thank the Texas Advanced Computing Center (TACC) and TeraGrid sponsored by the National Science Foundation for the computer time.

References

1. Adler K, Brücker C. Dynamic flow in a realistic model of the upper human lung airways. *Exp. Fluids*. 2007; 43:411–423.
2. ARDSN: The Acute Respiratory Distress Syndrome Network (ARDSN). Ventilation with lower tidal volumes as compared with traditional tidal volumes for acute lung injury and the acute respiratory distress syndrome. *N. Engl. J. Med.* 2000; 342:1301–1308. [PubMed: 10793162]
3. Chang HK. Mechanisms of gas transport during ventilation by high-frequency oscillation. *J. Appl. Physiol.* 1984; 56:553–563. [PubMed: 6368498]
4. Choi J, Tawhai MH, Hoffman EA, Lin C-L. On intra- and intersubject variabilities of airflow in the human lungs. *Phys. Fluids*. 2009; 21:101901. DOI: 10.1063/1.3247170.
5. Darquenne C, Kim Prisk G. Aerosols in the study of convective acinar mixing. *Respir. Physiol. & Neurobiol.* 2005; 148(1-2):207–216. [PubMed: 15890563]
6. Derdak S, Mehta S, Stewart TE, Smith T, Rogers M, Buchman TG, Carlin B, Lowson S, Granton J, the Multicenter Oscillatory Ventilation for Acute Respiratory Distress Syndrome Trial (MOAT) Study Investigators. High-frequency oscillatory ventilation for acute respiratory distress syndrome in adults: a randomized, controlled trial. *Am. J. Respir. Crit. Care Med.* 2002; 166:801–808. [PubMed: 12231488]
7. Dos Santos CC, Slutsky AS. The contribution of biophysical lung injury to the development of bio-trauma. *Annu. Rev. Physiol.* 2006; 68:585–618. [PubMed: 16460285]
8. Formaggia L, Nobile F, Quarteroni A, Veneziani A. Multiscale modelling of the circulatory system: a preliminary analysis. *Comput. Visual. Sci.* 1999; 2:2–3.

9. Grinberg L, Karniadakis G. Outflow boundary conditions for arterial networks with multiple outlets. *Ann. Biomed. Eng.* 2008; 36:9.
10. Henry FS, Butler JP, Tsuda A. Kinematically irreversible acinar flow: a departure from classical dispersive aerosol transport theories. *J. Appl. Physiol.* 2002; 92:835–845. [PubMed: 11796699]
11. Heraty KB, Laffey JG, Quinlan NJ. Fluid Dynamics of Gas Exchange in High-Frequency Oscillatory Ventilation: In Vitro Investigations in Idealized and Anatomically Realistic Airway Bifurcation Models. *Ann. Biomed. Eng.* 2008; 36(11):1856–1869. [PubMed: 18785010]
12. Heyder J, Blanchard JD, Feldman HA, Brain JD. Convective mixing in human respiratory tract: estimates with aerosol boli. *J. Appl. Physiol.* 1988; 64:1273–1278. [PubMed: 3366742]
13. Horsfield K, Dart G, Olson DE, Filley GF, Cumming G. Models of the human bronchial tree. *J. Appl. Physiol.* 1971; 31:207–217. [PubMed: 5558242]
14. Jan DL, Shapiro AH, Kamm RD. Some features of oscillatory flow in a model bifurcation. *J. Appl. Physiol.* 1989; 67:147–159. [PubMed: 2759939]
15. Krishnan JA, Brower RG. High frequency ventilation for acute lung injury and ARDS. *Chest.* 2000; 118:795–807. [PubMed: 10988205]
16. Kumar H, Tawhai MH, Hoffman EA, Lin C-L. The effects of geometry on airflow in the acinar region of the human lung. *J. Biomech.* 2009; 42:1635–1642. [PubMed: 19482288]
17. Lieber BB, Zhao Y. Oscillatory flow in a symmetric bifurcation airway model. *Ann. Biomed. Eng.* 1998; 26:821–830. [PubMed: 9779955]
18. Lin C-L, Lee H, Lee T, Weber LJ. A level set characteristic Galerkin finite element method for free surface flows. *Int. J. Numer. Meth. Fluids.* 2005; 49(5):521–547.
19. Lin C-L, Tawhai MH, McLennan G, Hoffman EA. Characteristics of the turbulent laryngeal jet and its effect on airflow in the human intra-thoracic airways. *Respir. Physiol. & Neurobiol.* 2007; 157:295–309. [PubMed: 17360247]
20. Lin C-L, Tawhai MH, McLennan G, Hoffman EA. Multiscale simulation of gas flow in subject-specific models of the human lung. *IEEE Eng. in Med. and Bio.* 2009; 28:25–33.
21. Lunkenheimer PP, Rafflenbeul W, Keller H, Frank I, Dickhut HH, Fuhrmann C. Application of transtracheal pressures oscillations as modification of “diffusion respiration”. *Br. J. Anaesth.* 1972; 44:627. [PubMed: 5045565]
22. Ma B, Lutchen KR. An anatomically based hybrid computational model of the human lung and its application to low frequency oscillatory mechanics. *Ann. Biomed. Eng.* 2006; 34(11):1691–1704. [PubMed: 17019619]
23. Mackley MR, Neves Saraiva RMC. The quantitative description of fluid mixing using Lagrangian- and concentration-based numerical approaches. *Chem. Eng. Sci.* 1999; 54:159–170.
24. Majumdar A, Alencar AM, Buldyrev SV, Hantos Z, Lutchen KR, Stanley HE, Suki B. Relating airway diameter distributions to regular branching asymmetry in the lung. *Phys. Rev. Lett.* 2005; 95:168101. [PubMed: 16241843]
25. Marchak BE, Thompson WK, Duffty P, Miyaki T, Bryan MH, Bryan AC, Froese AB. Treatment of RDS by high-frequency oscillatory ventilation: a preliminary report. *J. Pediatr.* 1981; 99:287–292. [PubMed: 7252695]
26. Marini JJ. Evolving concepts in the ventilatory management of acute respiratory distress syndrome. *Clin. Chest Med.* 1996; 17:555–575. [PubMed: 8875011]
27. Mehta S, Granton J, MacDonald RJ, Bowman D, Matte-Martyn A, Bachman T, Smith T, Stewart TE. High-frequency oscillatory ventilation in adults: the Toronto experience. *Chest.* 2004; 126:518–527. [PubMed: 15302739]
28. Moganasundram S, Durward A, Tibby SM, Murdoch IA. High-frequency oscillation in adolescents. *Br. J. Anaesth.* 2002; 88:708–711. [PubMed: 12067010]
29. Nagels MA, Cater JE. Large eddy simulation of high frequency oscillating flow in an asymmetric branching airway model. *Med. Eng. Phys.* 2009; 31:1148–1153. [PubMed: 19716332]
30. Ottino, JM. *The kinematics of mixing: stretching, chaos and transport.* Cambridge University Press; Cambridge; 1989.
31. Roberts, EPL. Ph.D. thesis. Department of Chemical Engineering, University of Cambridge; UK: 1992. Unsteady flow and mixing in baffled channels.

32. Roberts EPL, Mackley MR. The simulation of stretch rates for the quantitative prediction and mapping of mixing within a channel flow. *Chem. Eng. Sci.* 1995; 50:3727–3746.
33. Saric WS. Görtler vortices. *Annu. Rev. Fluid Mech.* 1994; 26:379.
34. Tanaka G, Ogata T, Oka K, Tanishita K. Spatial and temporal variation of secondary flow during oscillatory flow in model human central airways. *J. Biomech. Eng.* 1999; 121:565–573. [PubMed: 10633255]
35. Tawhai MH, Pullan AJ, Hunter PJ. Generation of an anatomically based three-dimensional model of the conducting airways. *Ann. Biomed. Eng.* 2000; 28:793–802. [PubMed: 11016416]
36. Tawhai MH, Hunter PJ, Tschirren J, Reinhardt J, McLennan G, Hoffman EA. CT-based geometry analysis and finite element models of the human and ovine bronchial tree. *J. Appl. Physiol.* 2004; 97:2310–2321. [PubMed: 15322064]
37. Tremblay LN, Slutsky AS. Ventilator-induced lung injury: from the bench to the bedside. *Intensive Care Med.* 2006; 32:24–33. [PubMed: 16231069]
38. Vignon-Clementel IE, Figueroa CA, Jansen KE, Taylor CA. Outflow boundary conditions for three-dimensional finite element modeling of blood flow and pressure in arteries. *Comput. Methods Appl. Mech. Engrg.* 2006; 195:3776–3796.
39. Vreman A. An eddy-viscosity subgrid-scale model for turbulent shear flow: Algebraic theory and applications. *Phys. Fluids.* 2004; 16(10):3670–3681.
40. Womersley JR. Method for the calculation of velocity, rate of flow and viscous drag in arteries when the pressure gradient is known. *J. Physiol.* 1955; 127:553–563. [PubMed: 14368548]
41. Xia G, Tawhai MH, Hoffman EA, Lin C-L. Airway Wall Stiffness and Peak Wall Shear Stress: A Fluid-Structure Interaction Study in Rigid and Compliant Airways. *Ann. Biomed. Eng.* 2010; 38(5):1836–1853. [PubMed: 20162357]
42. Yin Y, Hoffman EA, Lin C-L. Mass preserving nonrigid registration of CT lung images using cubic B-spline. *Med. Phys.* 2009; 36:4213–4222. [PubMed: 19810495]
43. Yin Y, Choi J, Hoffman EA, Tawhai MH, Lin C-L. Simulation of pulmonary air flow with a subject-specific boundary condition. *J. Biomech.* 2010 doi:10.1016/j.jbiomech.2010.03.048.
44. Zhang Z, Kleinstreuer C. Transient airflow structures and particle transport in a sequentially branching lung airway model. *Phys. Fluids.* 2002; 14:862–880.
45. Zhao Y, Lieber BB. Steady expiratory flow in a model symmetric bifurcation. *J. Biomech. Eng.* 1994; 116:318–323. [PubMed: 7799634]

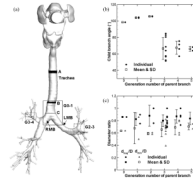


FIGURE 1.

(a) Front view of the CT-based airways (LMB, left main bronchus; RMB, right main bronchus). Solid, dot-dashed, and dashed boxes indicate the locations of selected bifurcations between G0-1, G2-3, and G3-4 (see Figs. 8-11), respectively. A and B denote particle released locations in HFOV and HFNR, respectively, for stretch rate analysis. C denotes the cross section where the CFD solutions computed on different mesh sizes are compared. (b) The distribution of the angle between child branches (degree) by generation. (c) The distribution of the ratio of the major (minor) child-branch diameter d_{maj} (d_{min}) over the parent-branch diameter D , d_{maj}/D (d_{min}/D), by generation. “Mean” and “SD” are the mean and the standard deviation of the child branch angles or the diameter ratios from individual bifurcations by generation.

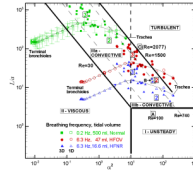
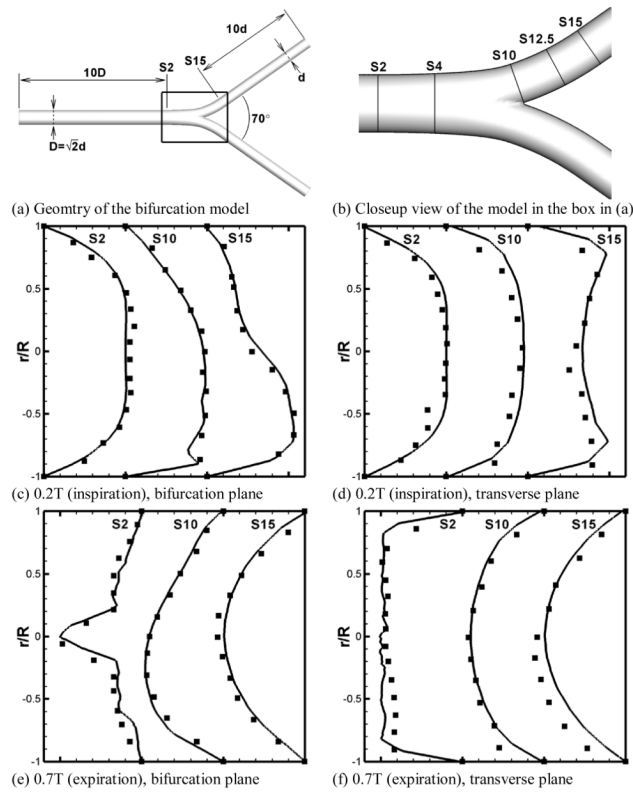


FIGURE 2.

Flow regimes of the conducting airway categorized based on a dimensionless frequency α^2 (α is Womersley number) and a dimensionless stroke length L/a . The (I) unsteady, (II) viscous, (IIIa, IIIb) convective flow regimes are classified according to Jan *et al.*¹⁴

**FIGURE 3.**

Comparison of velocity profiles in a single bifurcation with PIV measurements of Lieber and Zhao.¹⁷ Flow parameters correspond to point C in Fig. 2. Solid lines, current data; square symbols, PIV data. Bifurcation plane, co-planar with the centerlines of the branches; transverse plane, perpendicular to the bifurcation plane and one of the centerlines.

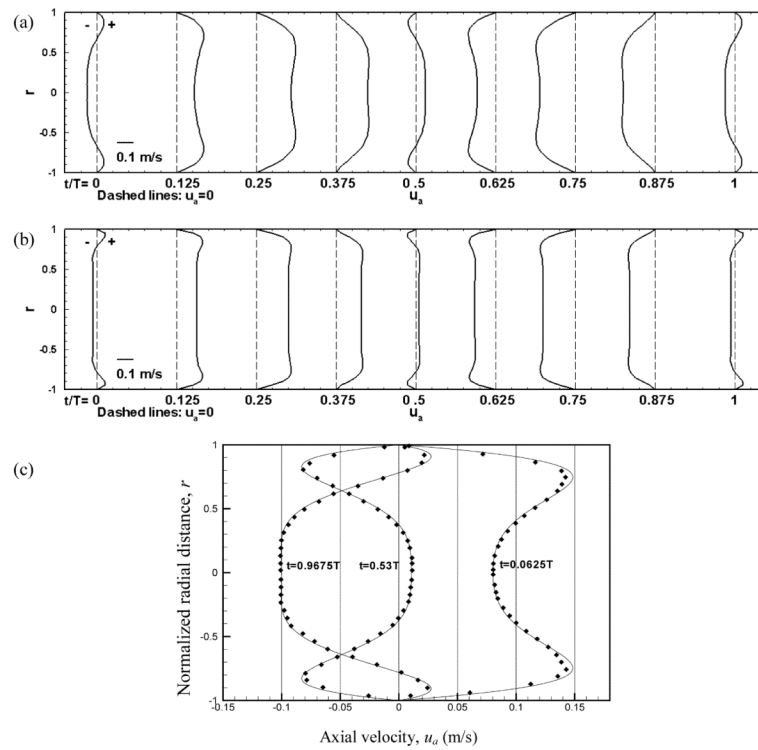


FIGURE 4. Analytical Womersley profiles at selected times during a cycle for the cases with $Re = 100$ and $\alpha =$: (a) 7 and (b) 14. (c) Comparison of CFD computed profiles (line) in a straight tube with the Womersley solution (symbol) for the case of $Re = 100$ and $\alpha = 7$.

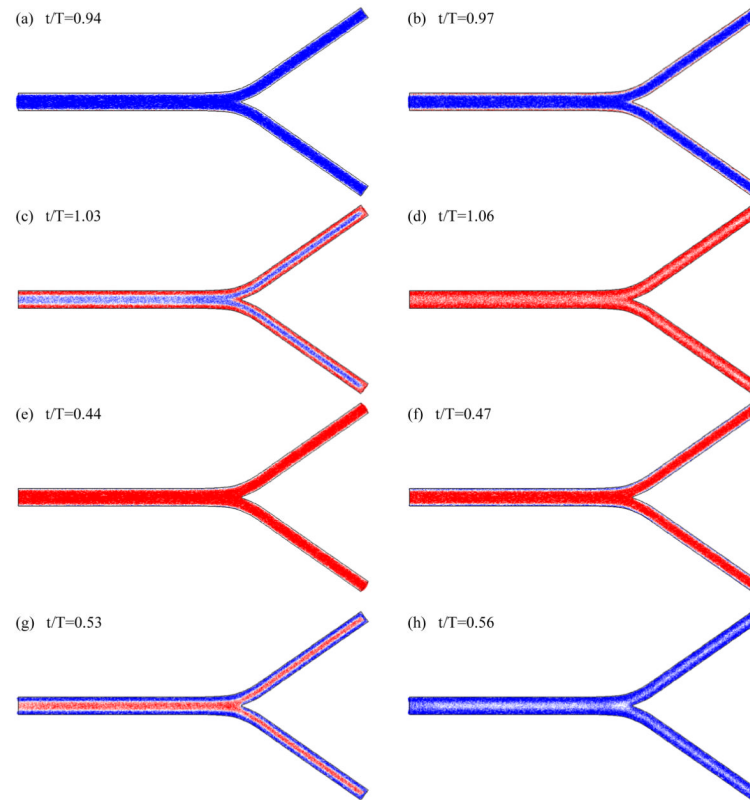


FIGURE 5.

A sequence of velocity distributions in the bifurcation plane with $Re = 100$, $L/a = 2$, $\alpha = 7$ (point A in Fig. 2). Blue, negative axial velocity to the left. Red, positive axial velocity to the right.

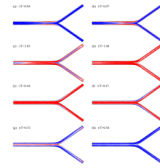


FIGURE 6.

A sequence of velocity distributions in the bifurcation plane at $Re = 740$, $L/a = 15$, $\alpha = 7$ (point B in Fig. 2). Blue, negative axial velocity to the left. Red, positive axial velocity to the right.

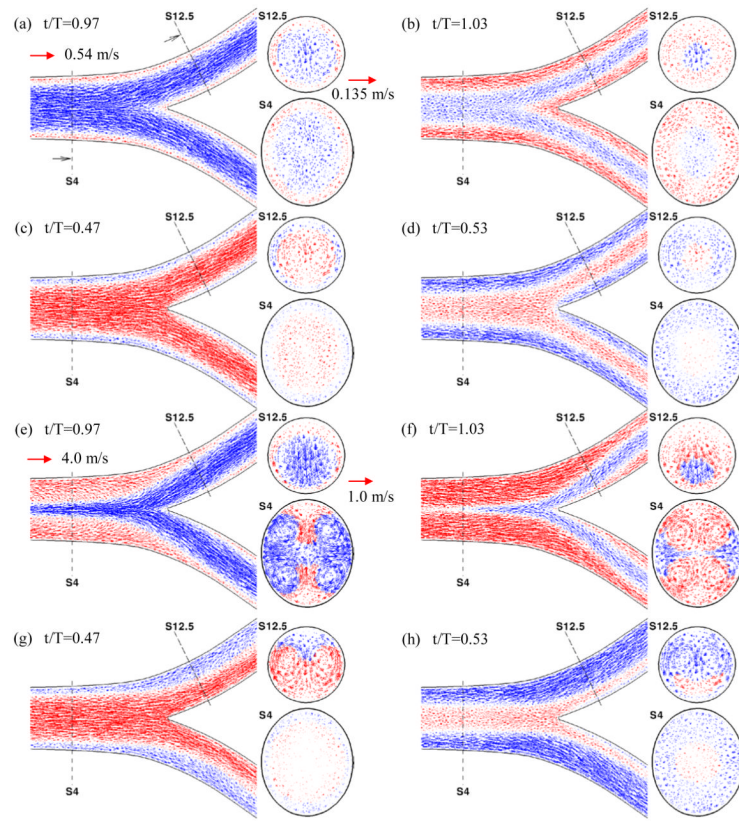


FIGURE 7. Close-up views of velocity vectors in Figs. 5 and 6 and two cross sections before and after flow reversal. (a)-(d), $Re = 100$; (e)-(h), $Re = 740$. Blue, negative axial velocity to the left; red, positive axial velocity to the right.

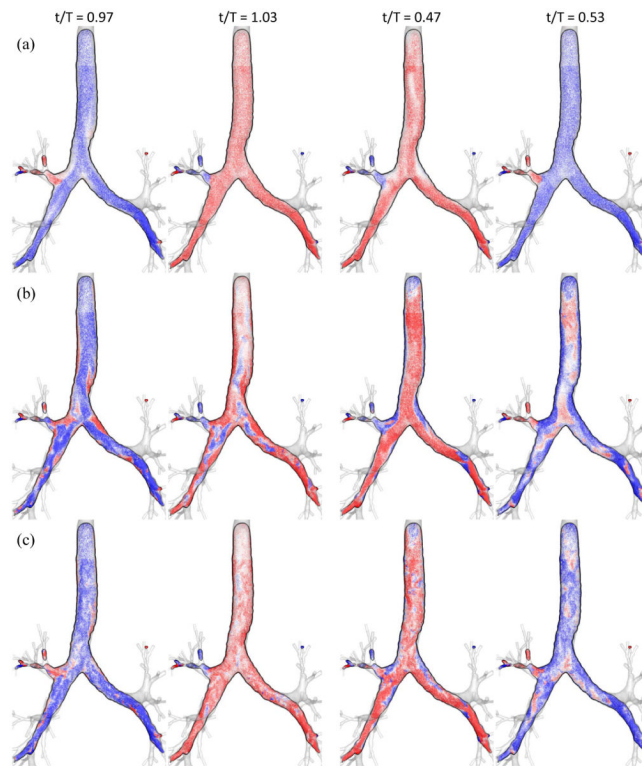


FIGURE 8. Velocity vectors in the bifurcation plane of the trachea and two main bronchi (G0-1) near flow reversal. Red, negative (downward) axial velocity; blue, positive (upward) axial velocity. (a) NORM, (b) HFNR and (c) HFOV. Instantaneous Reynolds numbers at the trachea are 241 for (a) and (b), and 684 for (c).

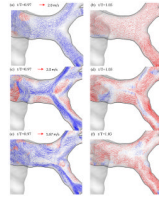


FIGURE 9.

Velocity vectors at end expiration and early inspiration in the bifurcation plane at the G2-3 bifurcation. Red (blue), positive (negative) axial velocity in the parent branch to the right (left). (a,b), NORM; (c,d), HFNR; (e,f), HFOV. Instantaneous Reynolds numbers at the parent branch (G2) are 64 for (a-d) and 182 for (e,f).

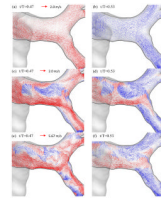


FIGURE 10.

Velocity vectors at end inspiration and early expiration in the bifurcation plane at the G2-3 bifurcation. Red (blue), positive (negative) axial velocity in the parent branch to the right (left). (a,b), NORM; (c,d), HFNR; (e,f), HFOV. Instantaneous Reynolds numbers at the parent branch (G2) are 64 for (a-d) and 182 for (e,f).

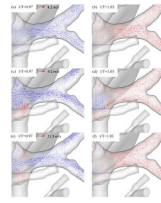


FIGURE 11.

Velocity vectors at end expiration and early inspiration in the bifurcation plane at the G3-4 bifurcation. Red (blue), positive (negative) axial velocity in the parent branch to the right (left). (a,b), NORM; (c,d), HFNR; (e,f), HFOV. Instantaneous Reynolds numbers at the parent branch (G3) are 52 for (a-d) and 147 for (e,f).

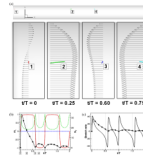


FIGURE 12.

Time histories of sample tracers and stretch rates in a straight tube. (a) Deformation of tracers at 4 normalized times $t/T = (0, 0.25, 0.60, 0.75)$ marked by (1, 2, 3, 4). (b) Time histories of orientation vector m_i released at $y/a = 0.48$ (the middle of the red line at $t/T = 0$). Subscript i (1, 2, 3) correspond to (x, y, z) in (red, green, blue). The black line with circle is the enlarged view of the s_T curve in (c). (c) Time histories of the stretch rates of a massless particle released at $y/a = 0.48$. Line, s_I (instantaneous stretch rate); line with circle, s_T (time-averaged stretch rate).

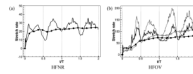
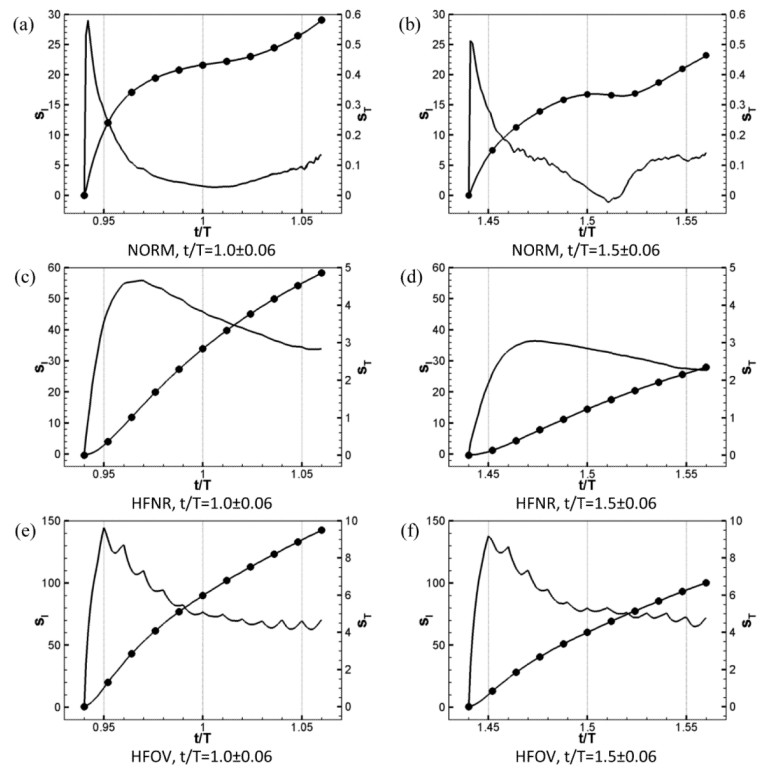


FIGURE 13.

Time histories of instantaneous and time-averaged stretch rates, s_T (line) and s_T (line with circle) for the whole airway cases: (a) HFNR and (b) HFOV. In (b), bold lines are based on the particles that remain active inside the model at the end of two cycles, whereas thin lines are based on the particles that are active at instant t/T . For (a) the distinction between bold and thin lines are negligible, thus only those based on active particles at the end of two cycles are shown.

**FIGURE 14.**

Time histories of instantaneous (s_I) and time-averaged (s_T) stretch rates near flow reversal for NORM, HFNR and HFOV at $t/T = 1 \pm 0.06$ (left panel) and $t/T = 1.5 \pm 0.06$ (right panel).

Table 1

Flow parameters for the three CT-based airway cases

| Case | Period T (s) | Frequency f (Hz) | Peak Re | Tidal volume V_T (ml) | Description |
|------|-------------------|-----------------------|-----------|----------------------------|---|
| NORM | 4.8 | 0.20 | 1288 | 500 | Normal breathing |
| HENR | 0.16 | 6.28 | 1288 | 16.58 | Same frequency as HFOV and same peak Re as NORM |
| HFOV | 0.16 | 6.28 | 3656 | 47 | High frequency oscillatory ventilation |

Table 2

Flow parameters for the two bifurcations in the CT-based airway model

| | L/a | α | α^2 | Peak Re | Local tidal volume (ml) |
|------------|--|----------|------------|-----------|-------------------------|
| Generation | A bifurcation between 2 nd -3 rd generations enclosed by a dot-dashed box in Fig. 1a | | | | |
| NORM | 163.4 | 1.45 | 2.10 | 343 | 73.1 |
| HFNR | 5.42 | 7.96 | 63.31 | 343 | 2.42 |
| HFOV | 15:36 | 7.96 | 63.31 | 972 | 6.87 |
| Generation | A bifurcation between 3 rd -4 th generations enclosed by a dotted box in Fig. 1a | | | | |
| NORM | 746 | 0.61 | 0.37 | 277 | 24.8 |
| HFNR | 24.7 | 3.35 | 11.2 | 277 | 0.82 |
| HFOV | 70.1 | 3.35 | 11.2 | 785 | 2.33 |